ARTICLE

Flexible freestanding all-MXene hybrid films with enhanced capacitive performance for powering flex sensor

Zhemin Li, [a] Yohan Dall'Agnese, [b] Jin Guo, [a] Haifu Huang, [a] Xianqing Liang [a] and Shuaikai Xu*[a]

Stacking different two-dimensional (2D) nanomaterials into composite structures opens an opportunity to fabricate electrodes combining the advantages of the individual nanomaterial. Here, different types of MXene nanosheets are combined to create flexible all-MXene hybrid films with high gravimetric capacitance and excellent rate performance for flexible supercapacitors. $Ti_3C_2T_x$ nanosheets are introduced in-between Nb_2CT_x layers, leading to a significantly increased interlayer spacing. The self-restacking of both types of MXenes nanosheets is effectively impeded, accelerating the diffusion of electrolyte ions and enabling more accessible 2D nanochannels. The freestanding $Ti_3C_2T_x/Nb_2CT_x$ films delivers a high gravimetric capacitance of 370 F g^{-1} at a scan rate of 2 mV s^{-1}, good rate performance with 56.1% capacitance retention at 200 mV s^{-1} and long cycle life. Furthermore, the energy density of the assembled all-solid-state symmetric supercapacitor can reach up to 5.5 mWh g^{-1} at power density of 141.4 mW g^{-1}. Serving as stable power source unit, the all-solid-state supercapacitor was also integrated with a flex sensor to fabricated self-powered device. The route to fabricate $Ti_3C_2T_x/Nb_2CT_x$ hybrid films with enhanced electrochemical performance is also applicable for other MXenes, promoting the applications of MXenes for flexible supercapacitors and integrated electronic devices.

1. Introduction

Flexible supercapacitors are playing an increasingly important role in energy storage due to their viability for flexible intelligent wearable electronic devices, which requires irregular power supply at different discharging rates. [1-3] Two-dimensional (2D) nanomaterials have gradually become potential electrode materials for flexible supercapacitors due to their atomic thickness and electrochemical active surface, especially they allow the development of binder-free flexible electrodes with improved capacitance.[4] 2D materials can provide slit-shaped ion diffusion channels that enable fast movement of electrolyte ions into the electrode bulk.[4]

In recent years, a new family of two-dimensional material called MXenes has been discovered, which are transition metal carbides and nitrides with a general formula of $M_{n+1}X_nT_x$, where M is an early transition metal, X represents C and/or N, T_x denotes surface functional groups, and n = 1, 2, or 3.[5-7] They can be generally obtained by selectively etching out the A atomic layers of corresponding MAX phase precursors.[8] The advantages of MXenes include to their metallic conductivity and hydrophilic surface. MXenes have proven to be promising candidates for supercapacitors with high specific capacitance under high charging rate, outperforming most previously reported materials.[1, 9-13] Among all MXenes, $Ti_3C_2T_x$ is the most widely studied because of its well established preparation

method and good conductivity.[6, 14-18] M. Ghidiu et al. reported a method of producing $Ti_3C_2T_x$ MXene using a solution of LiF/HCl, and the resulting additive-free $Ti_3C_2T_x$ films have volumetric capacitances of up to 900 F cm^{-3} in sulfuric acid with excellent cyclability and rate performances.[19] As with other two-dimensional materials, the restacking of the MXene nanosheets impedes the accessibility to electrolyte ions, hindering the full utilization of the whole electrode.[7] Introducing interlayer spacers between nanosheets is an effective and straightforward strategy to improve the electrochemical performance of MXenes.[20] For instance, carbon nanotubes, graphene and activated carbon have been combined with $Ti_3C_2T_x$ to fabricate flexible hybrid film electrodes with significantly improved electrochemical performance.[21-28]

Besides $Ti_3C_2T_x$, the studies of MXenes with a formula of M_2XT_x, for example Nb_2CT_x, are rarely reported for aqueous supercapacitors. M_2XT_x MXenes were generally used as anode materials for alkali metal-ion batteries or non-aqueous hybrid energy storage devices.[29-33] However, M_2XT_x MXenes may achieve higher specific capacitance than $Ti_3C_2T_x$. [34, 35] Theoretical calculation predicted Nb_2C to possess superior gravimetric and areal capacitances than Ti_3C_2. In Nb_2C MXene, Nb atomic layers surface of Nb_2C can be fully utilized, enabling sufficient redox sites when acting as intercalation pseudocapacitive electrodes. In addition, the Nb element in Nb_2CT_x possesses wider chemical valence than Ti element, providing higher electrochemical activity. However, higher reaction temperature and longer reaction time are often required to etch Nb_2AlC MAX by concentrated HF solution, causing that prepared Nb_2CT_x MXene to have more lattice defects and a smaller nanosheet size. [33, 34] As a result, the electrical conductivity of Nb_2CT_x is relatively lower than $Ti_3C_2T_x$, which limits Nb_2CT_x potential application in high power electrochemical energy storage.

a. Guangxi Colleges and Universities Key Laboratory of Novel Energy Materials and Related Technology, Guangxi Novel Battery Materials Research Center of Engineering Technology, Center on Nanoenergy Research, College of Physics Science and Technology, Guangxi University, Nanning 530004, P. R. China.
b. Institute for Materials Discovery, University College London, London WC1E 7JE, United Kingdom.
* Corresponding author. E-mail: skxu@gxu.edu.cn.

To overcome the limitations of individual 2D nanomaterial, combining different 2D materials in hybrid electrodes by alternating stacking can be an effective strategy. [36-39] Stacking different 2D materials into composite structures opens an opportunity to construct electrodes that would combine the advantages of the individual building blocks while eliminating the associated shortcomings.[38] Analogously, combining Nb_2CT_x MXene nanosheets with other 2D nanomaterials into composite structures could combine the advantages of the individual material, including high conductivity and high intercalation pseudocapacitance.[40] It has been reported that graphene, principally reduced graphene oxide (rGO), is a promising candidate to be assembled with MXene nanosheets into stacked 2D hybrid films.[23, 37] In our previous work, rGO was combined with $Ti_3C_2T_x$ to prepare $rGO/Ti_3C_2T_x$ films for supercapacitors. [26] However, the colloidal dispersion of graphene with hydrophobic surfaces in water is generally difficult to be achieved. In addition, the thermal reduction process to reduce graphene oxide is energy-intensive and deteriorate the mechanical strength of the hybrid films. In contrast to graphene, $Ti_3C_2T_x$ has high conductivity, hydrophilic surface and high intercalation pseudocapacitance.[41] Therefore, it would be an appropriate selection to stack $Ti_3C_2T_x$ with Nb_2CT_x nanosheets to fabricate flexible hybrid films with expected high capacitive performance. Moreover, the aqueous solution processing of hybrid suspension based on two-MXene nanosheets is favorable for the large-scalable preparation of MXene-based films.

In this work, we proposed the concept of all-MXenes hybrid films for the first time. We prepared Nb_2CT_x MXene at a lower reaction temperature and a shorter reaction time than previous report. [9, 31] Few-layer Nb_2CT_x nanosheets are obtained through manually shaking the multi-layer Nb_2CT_x intercalated by tetramethylammonium hydroxide (TMAOH). The simple vacuum filtration process is conducted to stack few-layer Nb_2CT_x and $Ti_3C_2T_x$ nanosheets layer by layer and fabricate flexible $Ti_3C_2T_x/ Nb_2CT_x$ hybrid films for ultrafast flexible supercapacitors. The resultant $Ti_3C_2T_x/Nb_2CT_x$ films efficiently alleviates the self-restacking of both $Ti_3C_2T_x$ and Nb_2CT_x nanosheets. In addition, the $Ti_3C_2T_x$ nanosheets intercalated between Nb_2CT_x nanosheets can act as conductive network while increasing the interlayer spacing of Nb_2CT_x, providing more accessible 2D nanochannels for electrolyte ions and ensuring high-rate performance. As a result, the flexible 2D hybrid film delivers improved capacitance up to 370 F g^{-1} at 2 mV s^{-1} with 56.1% capacitance retention at 200 mV s^{-1}, much higher than that of pure individual MXene films. Moreover, the assembled all-solid-state supercapacitor can yield an energy density of 5.7 mWh g^{-1} at power density of 171.5 mW g^{-1}. The all-solid-state supercapacitor presents excellent cyclability with 94% capacitance retention after 10,000 cycles. The assembled all-solid-state supercapacitor was used to supply a flex sensor, proving its potential for practical application in integrated intelligent wearable electronic devices.
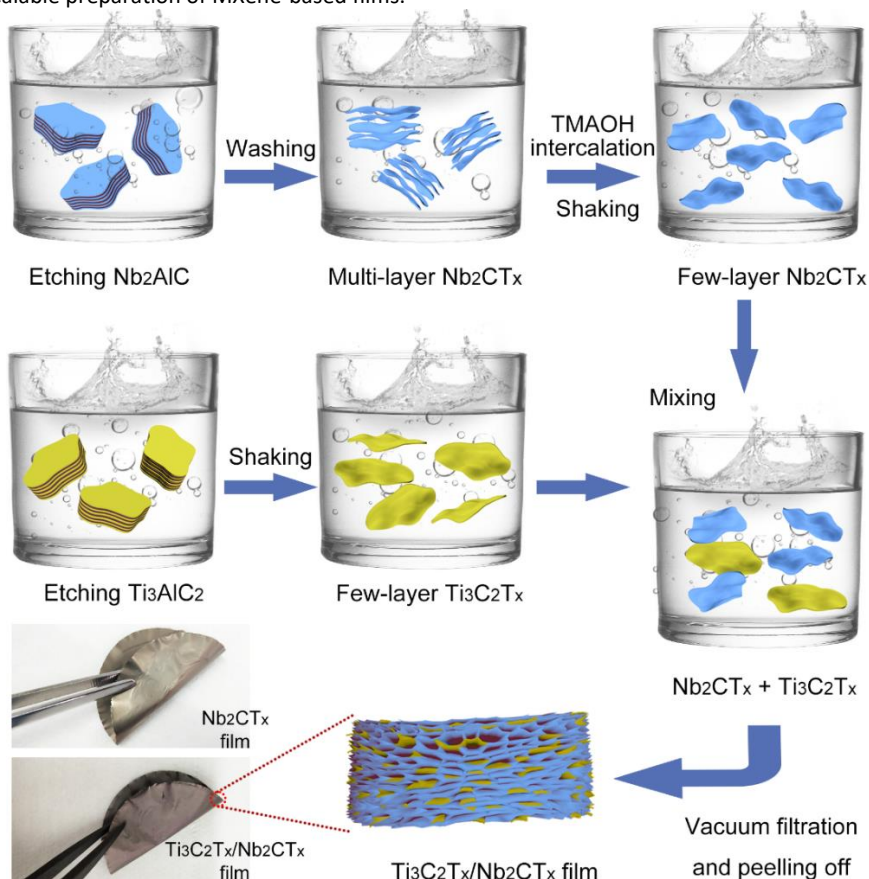

Fig. 1 The schematic of the fabrication process of flexible freestanding $Ti_3C_2T_x/Nb_2CT_x$ hybrid films, and the optical photographs of the prepared films.

ARTICLE

2. Results and discussion

Fig. 1 schematically illustrates the fabrication process of flexible hybrid $Ti_3C_2T_x/Nb_2CT_x$ film. Multi-layer Nb_2CT_x MXene was synthesized by HF etching of Nb_2AlC MAX phase. Organic polar TMAOH molecules were intercalated between Nb_2CT_x layers to enlarge the interlayer spacing, followed by manual shaking to delaminate Nb_2CT_x into few-layer nanosheets. The few-layer $Ti_3C_2T_x$ nanosheets were prepared according to the MILD method reported in the previous literature. [8] Finally, the flexible freestanding $Ti_3C_2T_x/Nb_2CT_x$ hybrid films with 5, 10, 30 or 50 wt% of $Ti_3C_2T_x$ nanosheets were obtained through vacuum-assisted filtration of the mixed few-layer $Ti_3C_2T_x/Nb_2CT_x$ suspension. The hybrid films are denoted as 5% T-N, 10% T-N, 30% T-N and 50% T-N, according to the weight percent of $Ti_3C_2T_x$ nanosheets in the hybrid films. The $Ti_3C_2T_x/Nb_2CT_x$ hybrid films possess good flexibility, as shown in the images in Fig. 1. After introducing $Ti_3C_2T_x$ into Nb_2CT_x films, the color of the hybrid films turns brown from initial champaign gold of pure Nb_2CT_x films.
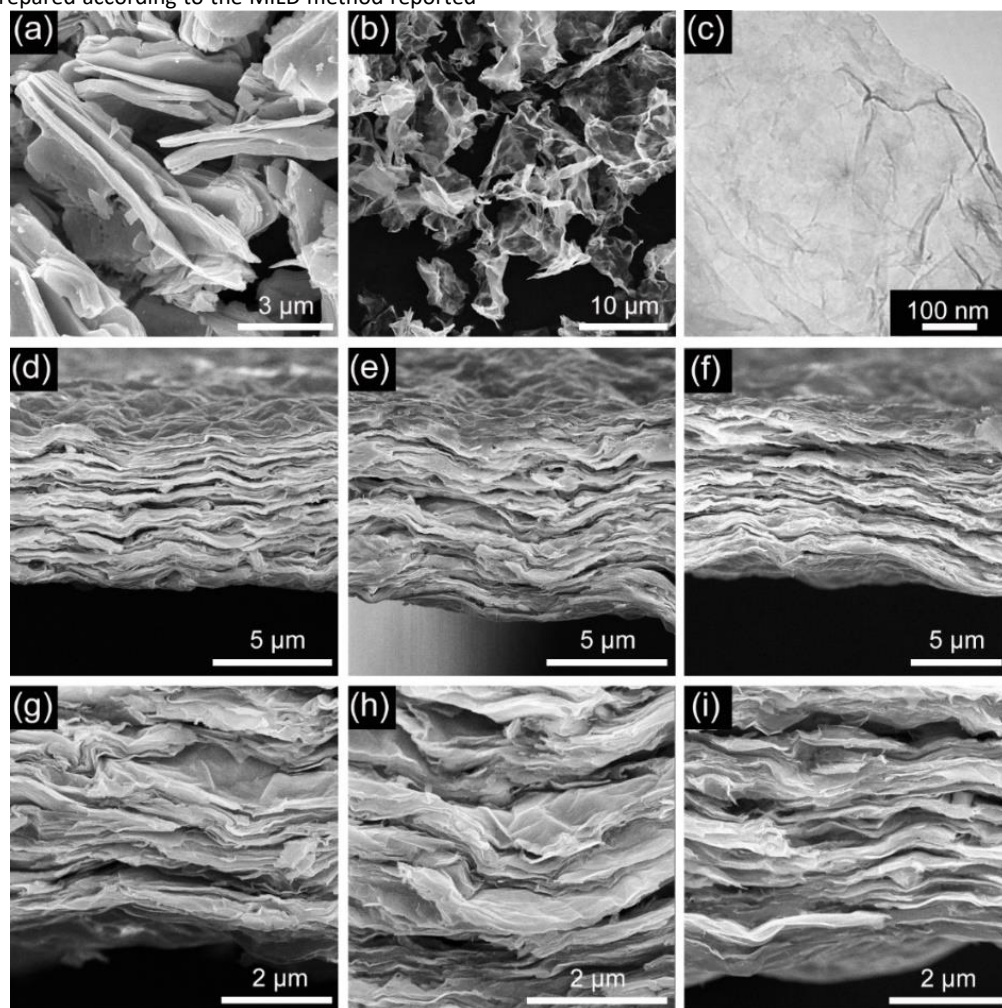
Fig. 2 (a, b) The typical SEM images of HF-etched multi-layer Nb_2CT_x MXene and delaminated few-layer Nb_2CT_x nanosheets, correspondingly. (c) TEM image of several Nb_2CT_x nanosheets, showing large lateral sizes. (d-f) Cross-sectional SEM images of the $Ti_3C_2T_x/Nb_2CT_x$ hybrid films with 5 wt%, 10 wt% and 30 wt% of $Ti_3C_2T_x$ in the hybrid films, correspondingly. (g-i) The high magnification SEM images of (d-f), correspondingly.

ARTICLE

Scanning electron microscopy (SEM) and transmission electron microscopy (TEM) were employed to define the morphology and microstructure of the obtained nanomaterials. After etching Al atom layers out from Nb_2AlC, the obtained multi-layer Nb_2CT_x present typical laminated structure as with the other MXenes, as shown in Fig. 2a. After delamination, the few-layer Nb_2CT_x nanosheets present thin lamellar morphology (Fig. 2b). It can be further demonstrated from the TEM result shown in Fig. 2c that the delaminated Nb_2CT_x nanosheets are successfully prepared. Fig. S3a shows the SEM result of delaminated $Ti_3C_2T_x$ nanosheets with larger lateral dimensions compared to Nb_2CT_x nanosheets. $Ti_3C_2T_x$ nanosheets were observed using TEM (Fig. S3b), confirming that the $Ti_3C_2T_x$ nanosheets are indeed few layers thick. So that when combining Nb_2CT_x with $Ti_3C_2T_x$ nanosheets, the introduction of $Ti_3C_2T_x$ nanosheets can improve the electrical conductivity of the whole hybrid film. The cross-sectional SEM image of the pure Nb_2CT_x film shown in Fig. S4a and b presents a well-aligned, layered structure. After combining with few-layer $Ti_3C_2T_x$ nanosheets, the obtained $Ti_3C_2T_x/Nb_2CT_x$ hybrid films with different weight percent of $Ti_3C_2T_x$ all maintained the similar layered structure of pure Nb_2CT_x film without any significant change, as shown in Fig. 2d-i and Fig. S4c, d. To clarify the homogeneous mixing degree of MXenes sheets in the films, EDS mapping images of the cross-sectional views of all samples are added, as shown in Fig. S5. It can be seen that the Ti and Nb elements are evenly distributed in the hybrid films, indicating that $Ti_3C_2T_x$ and Nb_2CT_x nanosheets are stacked homogeneously.

In order to analyze the material phases and the change of interlayer spacing between MXene nanosheets, X-diffraction (XRD) measurements were conducted on pure MXenes and hybrid films. As shown in Fig. S6a, after selective etching and delamination, the fabricated pure $Ti_3C_2T_x$ film presents a strong (002) diffraction peak at 6.7°, corresponding to an interlayer spacing of 1.31 nm, which is almost consistent with previously reported results.[10] As shown in Fig. S6b, it can be seen that the (002) diffraction peak shifts from 12.8° for Nb_2AlC MAX to 8.0° for multi-layer Nb_2CT_x due to the complete etching of Al atom layers. The (002) diffraction peak of freestanding Nb_2CT_x film further shifts to lower degree (7.6°) comparing to multi-layer Nb_2CT_x, which can be attributed to the intercalation of water and TMAOH between Nb_2CT_x nanosheets. When introducing $Ti_3C_2T_x$ nanosheets between Nb_2CT_x nanosheets, for example 10 wt% $Ti_3C_2T_x$, a new diffraction peak at 6.1° appears for 10% T-N, as shown in Fig. 3a and b. The increasing interlayer spacing between Nb_2CT_x nanosheets in 10% T-N due to the interaction with $Ti_3C_2T_x$ nanosheets should be responsible for this. On the other hand, the interlayer spacing between $Ti_3C_2T_x$ nanosheets in 10% T-N also significantly increased due to the compartment of Nb_2CT_x layers, resulting in the shift of (002) peak below 5°. The XRD patterns

of hybrid $Ti_3C_2T_x/Nb_2CT_x$ films with different content ratios are listed in Fig. 3c and d. With the increase of $Ti_3C_2T_x$ content from 5 to 30 wt%, the intensity of the diffraction peak at 6.2° gradually increases while the peak at 7.5° decreases, indicating a stepwise decrease in the degree of stacking order of Nb_2CT_x layers due to introducing of $Ti_3C_2T_x$ nanosheets. However, when the $Ti_3C_2T_x$ content increases to 50 wt%, the diffraction peak at 6.2° disappeared, which can be ascribed to the more intercalated $Ti_3C_2T_x$ nanosheets between Nb_2CT_x layers. In addition, it's worth noting the diffraction peak at 8.7°, which could be attributed to the residual thick Nb_2CT_x layers after delamination. Considering the close molecular weights of Nb_2CT_x and $Ti_3C_2T_x$, it can be estimated that $Ti_3C_2T_x$ is excessive for effective embedding between Nb_2CT_x layers in 50% T-N. The theoretical specific capacitance of Nb_2CT_x is higher than that of $Ti_3C_2T_x$ owing to the access to all transition metal layers and more abundant valence states of Nb atoms in Nb_2CT_x.[42] As a result, with the increase of $Ti_3C_2T_x$ content in the hybrid films from 5 to 30 wt%, the electrical conductivity increases gradually and the electrochemical active surfaces of Nb_2CT_x become more accessible to electrolyte ions, ensuring a high-power output during the fast charging and discharging processes. However, as for 50% T-N, its electrochemical active surfaces cannot be fully utilized due to the excess restacked $Ti_3C_2T_x$ nanosheets, leading to possible reduced electrochemical performance.
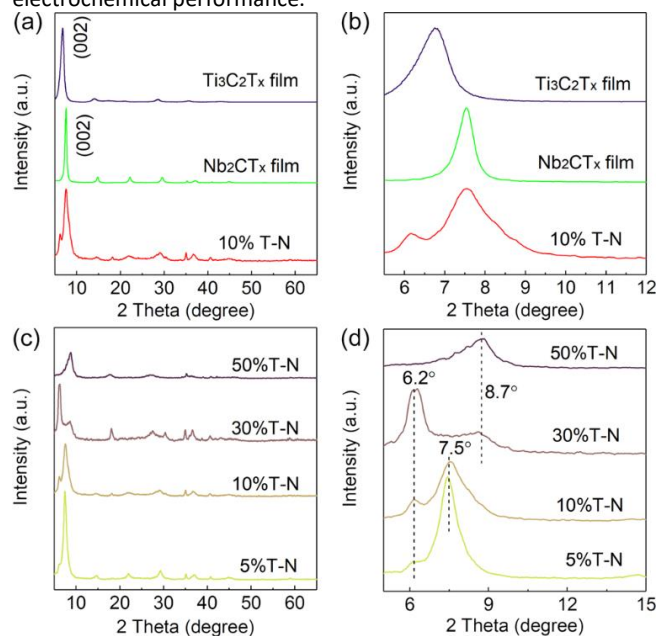
Fig. 3 (a-b) XRD patterns and magnified (002) peak region of the prepared $Ti_3C_2T_x$, Nb_2CT_x and 10% T-N films. (c-d) XRD patterns and magnified (002) peak region of the prepared hybrid $Ti_3C_2T_x/Nb_2CT_x$ films.

ARTICLE
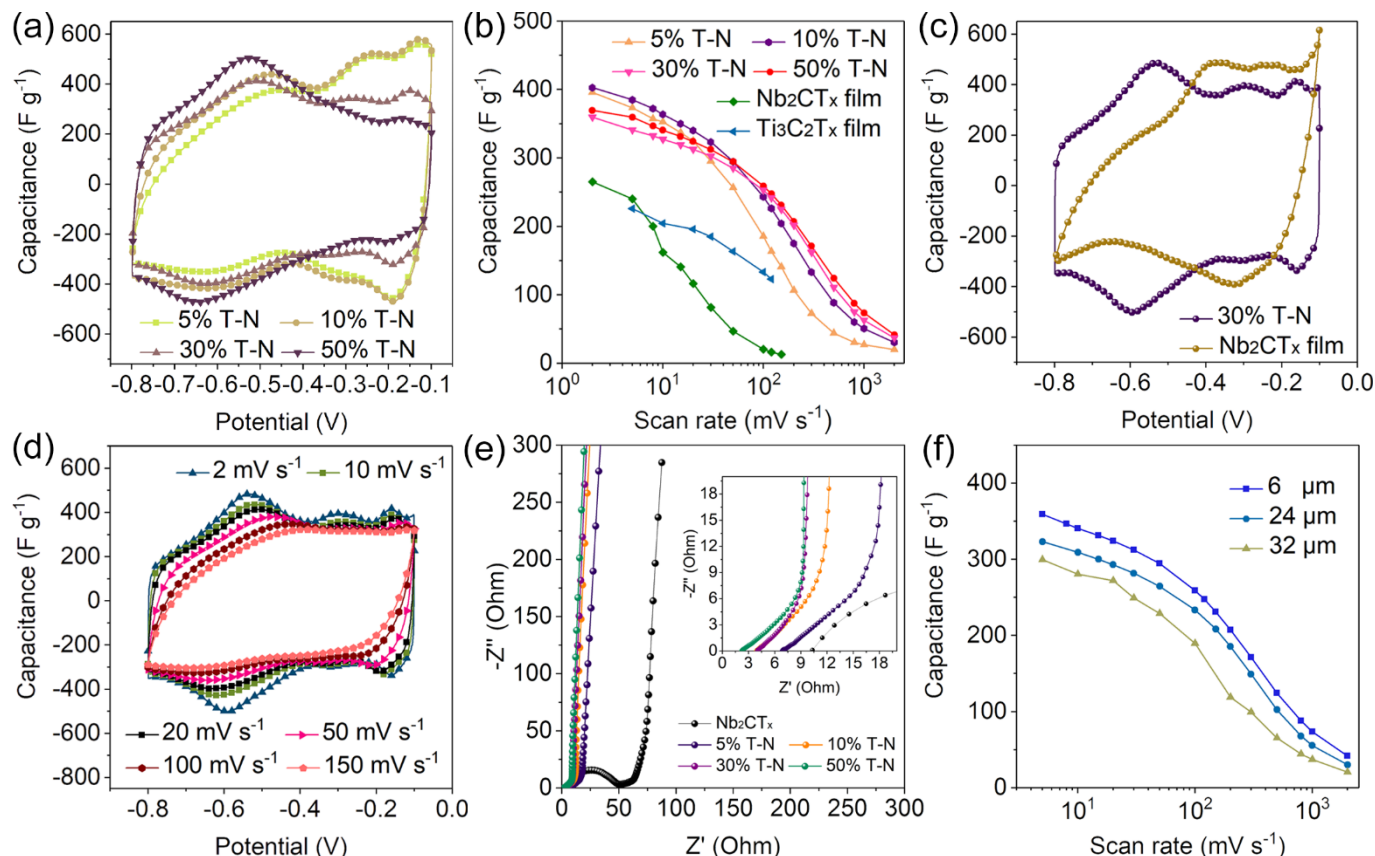
Fig. 4 Electrochemical performance of the prepared films in 2 M H_2SO_4 in a three-electrode configuration. (a) CV curves of $Ti_3C_2T_x/Nb_2CT_x$ hybrid films with different mass ratios of $Ti_3C_2T_x$ at a scan rate of 20 mV s^{-1}. (b) Rate performance of hybrid $Ti_3C_2T_x/Nb_2CT_x$, pure $Ti_3C_2T_x$ and Nb_2CT_x films at different scan rates. (c) Comparison of CV curves for 30% T-N and pure Nb_2CT_x films at a scan rate of 2 mV s^{-1}. (d) CV curves of the 30% T-N hybrid film at different scan rates. (e) Electrochemical impedance spectroscopy data of Nb_2CT_x and $Ti_3C_2T_x/Nb_2CT_x$ hybrid films. The inset in e shows the magnified high-frequency region. (f) The thickness-dependent electrochemical performance of 30% T-N hybrid film at different scan rates.

Compared to pure Nb_2CT_x film, the prepared Nb_2CT_x based hybrid films possess excellent flexibility and significantly increased interlayer spacing due to the introduction of $Ti_3C_2T_x$ nanosheets. Therefore, they are expected to present improved electrolyte ions accessibility, high specific capacitance and high rate capability, allowing them to be a potential candidate for flexible supercapacitors. The electrochemical performances of the $Ti_3C_2T_x/Nb_2CT_x$ films were characterized first in 2 M sulphuric acid (H_2SO_4) in a three-electrode configuration. The advantages of acidic electrolyte include excellent ionic conductivity and small size of protons known to allow for surface redox reactions.[19] The cyclic voltammetry (CV) curves of $Ti_3C_2T_x/Nb_2CT_x$ films with different $Ti_3C_2T_x$ contents at a scan rate of 20 mV s^{-1} are shown in Fig. 4a. The CV curves present three pairs of redox peaks in the entire potential window.

According to the previously reported results,[11] that pair of broad redox peaks below -0.4 V can be traced to the redox reaction occurred at the surface of $Ti_3C_2T_x$. The other two pairs of redox peaks above -0.4 V should be attributed to the pseudocapacitive behaviour of Nb_2CT_x. In acidic electrolyte, H^+ insertion into Nb_2CT_x can be expressed as: $Nb_2CT_x + yH^+ + ye^- \Leftrightarrow Nb_2CT_xH_y$ (y is the mole fraction of the inserted H^+). Considering the standard electrode potential of Nb element, the two pairs of redox peaks at about -0.15 and -0.28 V can be attributed to the redox reactions occurring at the surface of Nb_2CT_x, which change the oxidation state of Nb, in a similar way than what was observed in Ti_3C_2.

It can be observed that dominant redox peaks change with the increase of the introduced $Ti_3C_2T_x$. As for 30% T-N, its CV curves profiled quasi-rectangular shape, indicating that $Ti_3C_2T_x$

and Nb$_2$CT$_x$ almost contribute equivalent capacitance. The gravimetric capacitances of hybrid Ti$_3$C$_2$T$_x$/Nb$_2$CT$_x$, pure Ti$_3$C$_2$T$_x$ and Nb$_2$CT$_x$ films at different scan rates calculated from CV results were shown in Fig. 4b. After combining Nb$_2$CT$_x$ with Ti$_3$C$_2$T$_x$, the hybrid films exhibited significantly improved gravimetric capacitance compared to the pure MXene films, which are attributed to the increased interlayer spacing and improved electrolyte ions accessibility. At 2 mV s^{-1}, the gravimetric capacitance of 10% T-N can reach up to 403 F g^{-1}, while 265 and 245 F g^{-1} for pure Nb$_2$CT$_x$ and Ti$_3$C$_2$T$_x$ films, correspondingly. At 100 mV s^{-1}, the gravimetric capacitances of 5，10，30 and 50 % T-N films can retain 46.8, 60.3, 70.0 and 69.0 % retention of initial value at 2 mV s^{-1}, correspondingly. Among all hybrid films, 30% T-N possessed the best rate performance. Even at high scan rate of 300 mV s^{-1}, the capacitance of 30% T-N can still retain 46.6% of the value at 2 mV s-1. Considering the practical application potential, 30% T-N was regarded as the optimized hybrid film. From Fig. 4c, it can be seen that the CV curve of 30% T-N is closer to quasi rectangular than that of pure Nb$_2$CT$_x$ film, further demonstrating 30% T-N can store energy at constant rate in its entire potential window. Indeed, the high capacitance

contribution potential ranges of pure MXene films are compensated by each other, leading to the continuous high capacitive performance for hybrid 30% T-N in the entire potential window. The BET nitrogen adsorption-desorption isotherms and pore size distributions of the Nb$_2$CT$_x$ and all-MXene hybrid films were also measured, as shown in Fig. S7-9. With the increase of Ti$_3$C$_2$T$_x$ content, the BET surface area first increases and then decreases, with 30% T-N reaching the maximum, although all values are relatively close and low compared to activated carbon. The high capacitance obtained despite the low surface areas is another suggestion that the good performance is mostly due to the redox pseudocapacitance rather than electrostatic double layer capacitance. All the films possess ideal pore size distribution (around 4 nm, Fig. S7b, 8b) due to their two-dimensional stacking structure. The ICP analysis of the hybrid films was conducted and shown in Fig. S10. As expected, with the increase of the Ti$_3$C$_2$T$_x$ nanosheets in the hybrid films, the mass ratio of Ti element goes up. The insertion of a small amount of Ti$_3$C$_2$T$_x$ can significantly improve the electrochemical performance of the all-MXene hybrid films, demonstrating the importance of combining Ti$_3$C$_2$T$_x$ and Nb$_2$CT$_x$.
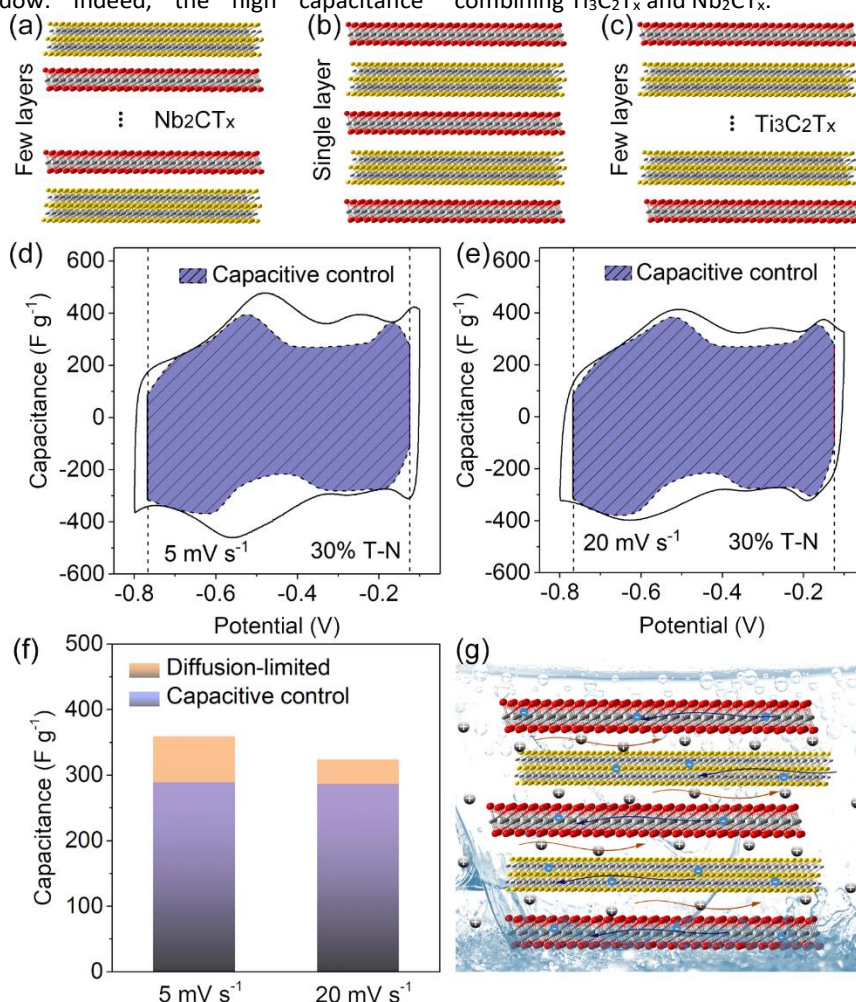
Fig. 5 (a-c) Schematic illustration of Ti$_3$C$_2$T$_x$/Nb$_2$CT$_x$ hybrid films showing the different layer ratios of Ti$_3$C$_2$T$_x$ to Nb$_2$CT$_x$. (d-e) Cyclic voltammetry profiles collected at 5 mV s^{-1} and 20 mV s^{-1} with hatched portions of the contributions of the processes not limited by diffusion.

(f) The capacitive control and diffusion-limited contributions of the hybrid films, (g) The schematic diagram of the 30% T-N used as electrode.

From the CV curves of 30% T-N shown in Fig. 4d, it can be seen their integral areas at scan rates from 2 to 50 mV s^{-1} have no significant changes. Even at 100 and 150 mV s^{-1}, the CV curves still remain the similar quasi-rectangular shape, indicating 30% T-N possesses excellent rate performance. Fig. S11 represents the galvanostatic charge/discharge (GCD) curves of the 30% T-N between -0.8 and -0.1 V at different current densities from 0.5 to 10 A g^{-1}. It can be observed that the GCD curves are almost linear and close to triangular shape, further confirming that hybrid 30% T-N exhibited a typical capacitive characteristic, which is in consistent with the result of CV curves. In order to verify the effect of the $Ti_3C_2T_x$ content on the electrochemical performance of the hybrid films, their electrochemical impedance spectroscopy (EIS) was performed at the same bias voltage of -0.3 V, as shown in Fig. 4e. The electrical equivalent circuit shown in Fig. S12 was used for fitting the impedance spectras. The detail fitting results are presented in Table S1. With the increase of $Ti_3C_2T_x$ content, the equivalent series resistance of the hybrid films decreased gradually, indicating the increase of their conductivity. However, the 45° angle section corresponding to ion migration limitation and charge transfer resistance of the hybrid films decreased first, but then increased, with the minima obtained with 30% T-N reached. The low charge transfer resistance supports 30% T-N optimal rate performance. In the low frequency region, all the EIS curves represented linear vertical profile, demonstrating that introducing of $Ti_3C_2T_x$ nanosheets is favorable for the ions diffusion and transport.

Previously reported excellent energy storage performance of MXene based films is mostly based on thin electrode thickness. However, the development of thick film electrodes with high gravimetric capacitance is critical to the practical application of supercapacitors. Therefore, the electrochemical responses of hybrid 30% T-N films with different thicknesses were compared, as shown in Fig. 4f. Although the gravimetric capacitances decreased with increased thickness, a high capacitance of 300 F g^{-1} remained for the 32-μm-thick 30% T-N film, and 63.3% capacitance retention of that at 2 mV s^{-1} can be retained at high scan rate of 100 mV s^{-1}. The high gravimetric capacitance and good rate performance of the 32-μm-thick 30% T-N film demonstrates the combination of different MXenes can be an effective approach to improve the electrochemical performance of MXene based films for application as negative electrodes of hybrid large-scale energy storage devices.

In order to further investigate the effect of the $Ti_3C_2T_x$ content on the electrochemical performances of hybrid films, the layer ratio of $Ti_3C_2T_x$ to Nb_2CT_x in the hybrid electrodes were calculated. When the $Ti_3C_2T_x$ content percent was low, for example 5 and 10% T-N, the Nb_2CT_x nanosheets can't be separated from each other by the introducing $Ti_3C_2T_x$ nanosheets, as schematically shown in Fig. 5a. Taking account of the similar molecular weight of $Ti_3C_2T_x$ to Nb_2CT_x, optimal hybrid structure can be theoretically achieved when the content percent of both MXenes are almost equal, that is 50% T-N.

However, from the above XRD results (Fig. 3d) it can be estimated that in this work the delaminated Nb_2CT_x nanosheets are partially not exactly single-layer. As a result, the $Ti_3C_2T_x$ nanosheets in 50% T-N are excessive, causing the restacking of $Ti_3C_2T_x$, which schematic illustration is shown in Fig. 5c. Compared to 50% T-N, the layer ratio of $Ti_3C_2T_x$ to Nb_2CT_x in the hybrid 30% T-N is probably closer to 1:1 (Fig. 5b) and the amount of $Ti_3C_2T_x$ is just enough, ignoring the partial thick Nb_2CT_x layers. The optimized layer ratio in 30% T-N makes it have high specific capacitance and good rate performance. To quantify the capacitive and diffusion limited contributions to the total capacitances of 30% T-N, the Dunn's differentiation method was used.[19] From the results summarized in Fig. 5 d-e, it can be observed that, at low scan rate of 5 mV s^{-1}, there is about 81% contribution of capacitive control processes to the total capacitance. At a scan rate of 20 mV s^{-1}, the capacitive control contribution percent increased up to 90%. The capacitive-control and diffusion-limited contributions were evaluated and presented in Fig. 5f. These analysis results demonstrate that the total capacitances of 30% T-N derived mainly from surface capacitive effects, whether electrostatic or near-surface pseudocapacitive, which is benefited from the increased interlayer spacing and improved electrolyte ions accessibility due to the synergistic effect between $Ti_3C_2T_x$ and Nb_2CT_x in the hybrids. As shown in Fig. 5g, the enhanced electrochemical performances of hybrid 30% T-N such as high gravimetric capacitance and good rate performance can be attributed to the following aspects: (1) intercalation of $Ti_3C_2T_x$ nanosheets between Nb_2CT_x layers could effectively impede the self-restacking of Nb_2CT_x nanosheets while greatly increase the interlayer spacing of Nb_2CT_x layers. (2) the $Ti_3C_2T_x$ nanosheets with large lateral sizes could act as conductive network and improve the mechanical strength of whole hybrid films. (3) the well-aligned alternating ordered structures of the hybrid films are favorable to electrolyte ions to rapidly diffuse and transport in hybrid film electrodes during the charge/discharge processes, leading to enhanced electrochemical surface utilization of MXene nanosheets.

The supercapacitors in 2 M H_2SO_4 electrolyte based on 30% T-N were fabricated. Fig. 6a shows the CV curves of 30% T-N-based supercapacitors in 2 M H_2SO_4 at different scan rates. It can be seen that all the CV curves represent quasi-rectangle profiles, confirming that the supercapacitors exhibit typical capacitive performance. With the increase of scan rate, the CV curves maintain similar shapes without any obvious distortion, demonstrating promising rate capabilities. At 5 mV s^{-1}, the supercapacitor delivered a specific capacitance of 88 F g^{-1}. And even at 100 mV s^{-1}, 55.3% capacitance retention can be maintained. As shown in Fig. S13, the GCD curves of 30% T-N based supercapacitors in 2 M H_2SO_4 at different current densities are linear and close to triangular shape, which are in accordance with the CV curves results in Figure 6a.

In addition, all-solid-state supercapacitors based on 30% T-N were assembled with PVA-H_2SO_4 gel electrolyte. Obviously, the CV curves shown in Fig. 6b gradually deviated from the quasi-rectangle profile with the increase of scan rate, which can be attributed to the limited ion penetration of the hybrid film electrodes. However, the

all-solid-state supercapacitor delivered a specific capacitance of 81 F g^{-1} at 5 mV s^{-1}, and 37 F g^{-1} at 100 mV s^{-1}. As shown in Fig. 6c, the discharging curves of the all-solid-state supercapacitor at different current densities maintained linear profiles, indicating typical capacitive characteristic. To investigate the flexibility of the assembled all-solid-state supercapacitor, its CV curves under different bending degrees are recorded and shown in Fig. 6d. It can be observed that the CV curves of the all-solid-state supercapacitor showed perfectly overlapped and negligible capacitance degradation at different bending angles, indicating the excellent mechanical stability and flexibility. To further investigate the potential of the assembled all-solid-state supercapacitor applications, the long-term cycling stability was evaluated by repeating the GCD test at 2 A g^{-1} for 10,000 cycles. After 10,000 charging/discharging cycles, the capacitance retention can maintain 94%, demonstrating that the all-solid-state supercapacitors exhibit excellent cycling stability (Fig. 6e). The slight capacitance losses observed after 6000 cycles can be

attributed to partially irreversible redox reactions, which might potentially lead to oxidation and degradation of Nb_2CT_x. Moreover, the electrochemical performance of the assembled 30% T-N based supercapacitors in this work were compared with other state-of-the-art MXene-based supercapacitors, as shown in the Ragone plots in Fig. 6f. The energy density of the supercapacitor in 2 M H_2SO_4 can reach 5.7 and 2.3 mWh g^{-1} at power density of 172.5 and 3000.0 mW g^{-1}, respectively. As for the all-solid-state supercapacitor with PVA-H_2SO_4, 5.5 and 1.1 mWh g^{-1} can be delivered at 141.4 and 2350.0 mW g^{-1}, respectively. Compared to the previous reported MXene-based and carbon-based supercapacitors, the $Ti_3C_2T_x/Nb_2CT_x$ based supercapacitors in this work can deliver high energy densities at high power densities, which ensures them serve as promising power source units for wearable electronics applications. The detailed comparison results were listed in Table S2 and S3 in supporting information.
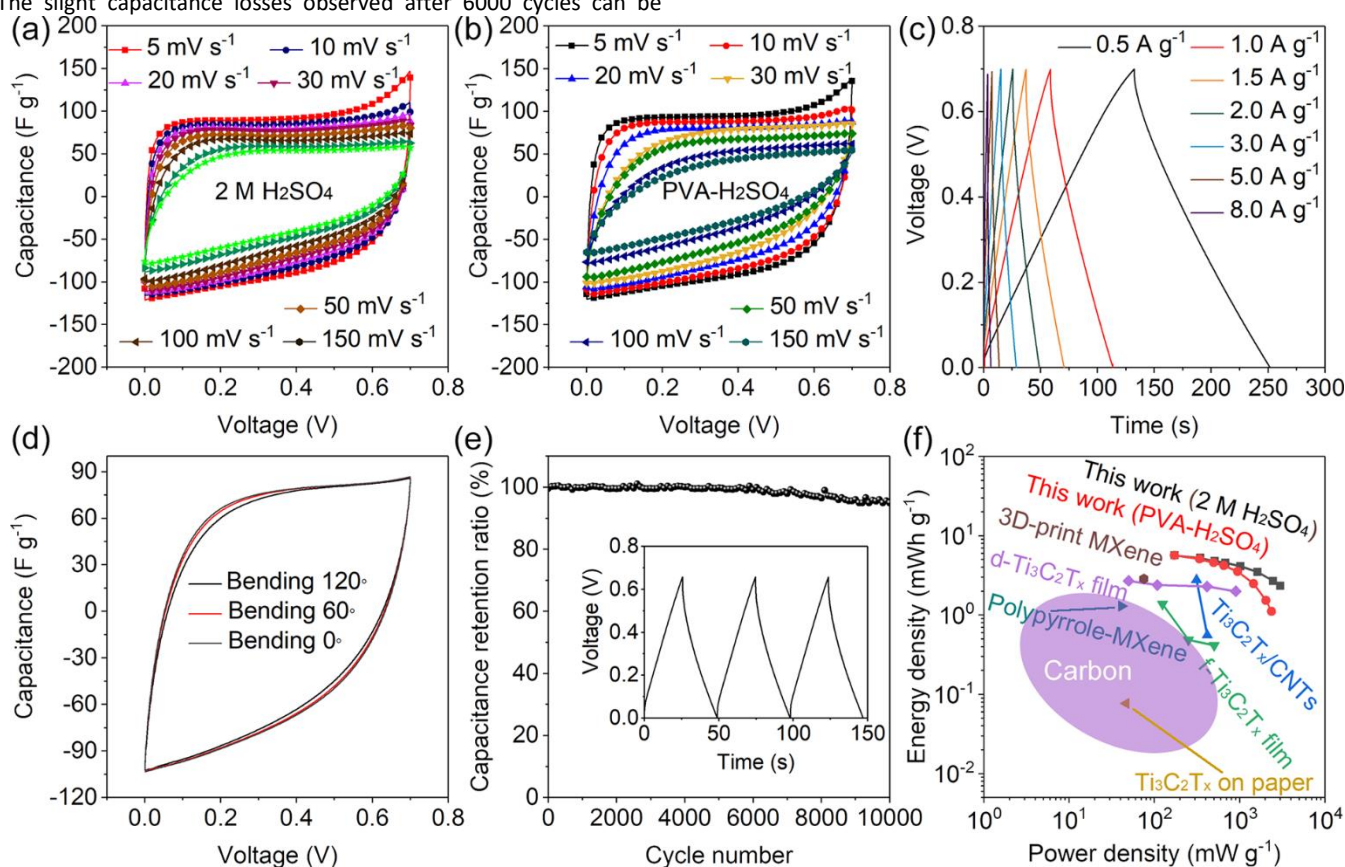
Fig. 6 Electrochemical performance of the fabricated supercapacitors. CV curves of 30% T-N-based supercapacitors (a) in 2 M H_2SO_4 electrolyte and (b) with PVA-H_2SO_4 gel at different scan rates. (c) GCD curves of 30% T-N-based supercapacitors with PVA-H_2SO_4 gel at different current densities. (d) CV curves of the all-solid-state supercapacitors bended at different angles of 0°, 60° and 120° at 30 mV s^{-1}. (e) The capacitance retention of the all-solid-state supercapacitors after 10, 000 cycles at 2 A g^{-1}. The inset is the last three charge-discharge cycles. (f) Ragone plots of the fabricated supercapacitors in this work and the other state-of-the-art MXene-based and carbon-based supercapacitors from the literature.

To further explore the practical application of the fabricated all-solid-state supercapacitors in portable electronic devices, we integrated the flex sensor together with the supercapacitor to fabricate integrated self-powered sensing devices, which schematic illustration is shown in Fig. 7a. The flex sensor was connected in

series with the supercapacitor, where the all-solid-state supercapacitor serves as power source of the integrated device, as shown in the schematic circuit diagram (Fig. 7a). The flex sensor is basically a variable resistor that reacts to bends, which resistance increases with the increasing bending degree. Under different

bending angles, the current response in the circuit is not the same, indicating the bending degree of the device. The working principle diagram of the flex sensor is shown in Fig. S14. From the self-discharge curve of the all-solid-state supercapacitor shown in Fig. 7b, it can be seen that the open-circuit voltage can remain about 0.5 V after 1000 s, confirming the feasibility to use it as power source to drive the flex sensor. The integrated flex sensor can be used to detect the finger bending angle, as shown in Fig. 7c. When the finger bended and relaxed, the movements could be tracked by the integrated flex

sensor and subsequently transformed into electronic output. To acquire the current response value at each bending angle, the current responses of the integrated flex sensor for different bending angles were measured and presented in Fig. 7d. It can be observed that the sensing response intensity increased with the increasing bending degrees from 30° to 180°. All of the above experimental results indicate the $Ti_3C_2T_x/Nb_2CT_x$-based all-solid-state supercapacitor can be used as stable power source units for portable electronic devices and medical microdevices.
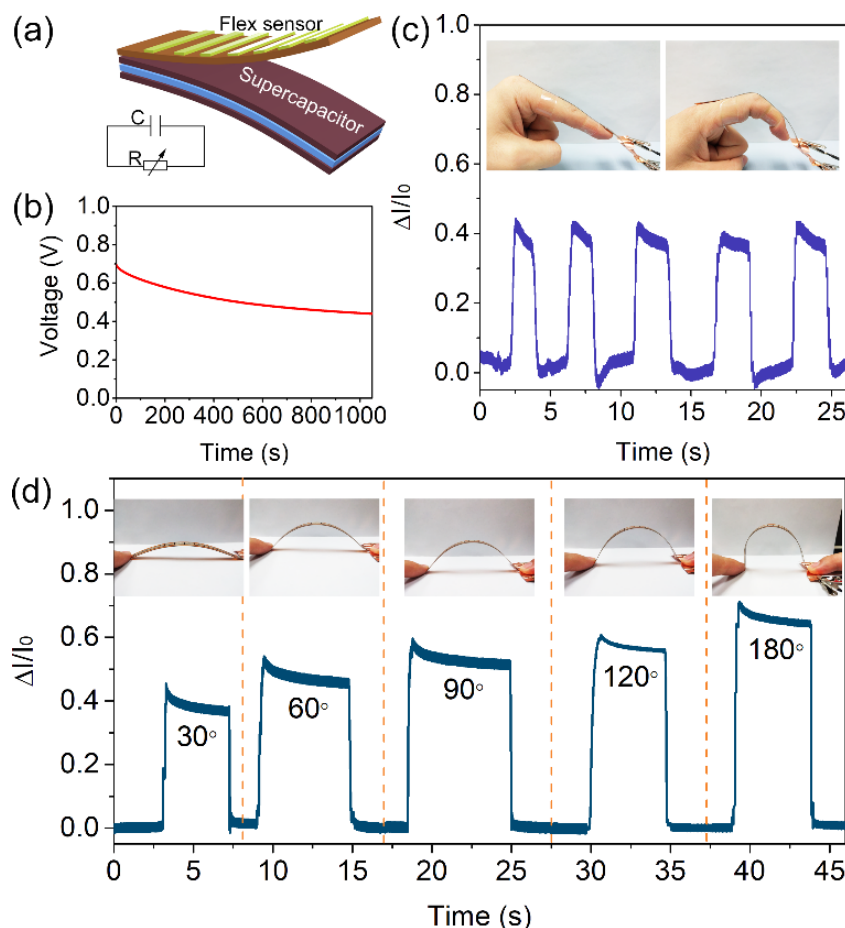
Fig. 7 (a) Schematic illustration of the integrated self-powered flex sensor, where the all-solid-state supercapacitor serves as power source. (b) The self-discharge curve of the all-solid-state supercapacitor. (c) Sensing responses for finger joint movement. (d) Sensing responses of the integrated flex sensor for different bending angles. ΔI denotes the change of the current before and after the bending, and I_0 is the current when no bending is applied.

3. Conclusions

In summary, it's proposed that stacking few-layer Nb_2CT_x with $Ti_3C_2T_x$ nanosheets into composite structures is a simple and effective approach to improve the electrochemical performance of Nb_2CT_x-based films for supercapacitors. The intercalated $Ti_3C_2T_x$ nanosheets between Nb_2CT_x layers effectively increase the interlayer spacing of Nb_2CT_x layers and impede the self-restacking of Nb_2CT_x nanosheets, which are favorable to electrolyte ions to rapidly diffuse and transport in the hybrid electrodes. The optimized $Ti_3C_2T_x/Nb_2CT_x$ films possess enhanced capacitive performance and rate

performance. A gravimetric capacitance of 370 F g^{-1} can be delivered at 2 mV s^{-1}, and 56.1 % capacitance retention at high scan rate of 200 mV s^{-1}. The energy density of the assembled all-solid-state supercapacitors can reach 5.5 mWh g^{-1} at power density of 141.4 mW g^{-1}, and 1.1 mWh g^{-1} at high power density of 2350.0 mW g^{-1}. The all-solid-state supercapacitors presented good flexibility and long cycling life. The all-solid-state supercapacitor was also integrated with a flex sensor to fabricated self-powered device, where all-solid-state supercapacitor served as stable power source unit to drive the flex sensor. The route to fabricate $Ti_3C_2T_x/Nb_2CT_x$ hybrid film is also applicable for other M_2CT_x MXenes, for example, Ti_2CT_x and

V_2CT_x, improving the application potential of MXenes for flexible supercapacitors and integrated electronic devices.

4. Experimental

4.1. Synthesis of Ti₃AlC₂ and Nb₂AlC phase

Ti_3AlC_2 was synthesized as described in our previous work.[14] Typically, TiH_2, Al, and TiC powders were mixed in 1: 1.2: 2 mole ratio, and ball milled for 24 h followed by sintering in a tube oven at 1450 °C in a corundum crucible and kept at that temperature for 2 h in a flowing Ar atmosphere. Crushing and sieving the resulting compact powder, Ti_3AlC_2 powder with size of < 38 μm was obtained. The Nb_2AlC powders were made by mixing elemental Nb, Al and C powders in a 2:1.1:1 molar ratio. The mixed powders were ball-milled for 12 h and cold-pressed into cylindrical discs. Then the discs were sintered at 1600 °C for 4 h in a flowing Ar atmosphere. Finally, the resultant discs were ball milled and sieved through a 400 mesh screen to obtain Nb_2AlC powder with particle size of < 38 μm.

4.2. Preparation of few-layer Ti₂C₂Tₓ suspension

Few-layer $Ti_3C_2T_x$ suspension was synthesized by etching Ti_3AlC_2 MAX powder in LiF/HCl hybrid etchant according to the previously reported route.[8] Typically, a total of 3.0 g of Ti_3AlC_2 precursor powder was gradually added (over the course of 5 min) to LiF (4.8 g)/HCl (60 mL, 9 M) mixture. Then the mixture was left under continuous stirring at room temperature for 24 h. Afterward, the resultant acidic mixture was washed copiously with deionized water via centrifugation at 3500 rpm several times for 5 min per cycle until a stable dark-green supernatant solution, with a pH of ≥ 6, was obtained. Adding water to the sediment and manually shaking it for several minutes, delaminated $Ti_3C_2T_x$ nanosheets can be obtained. After 1 h centrifugation at 3500 rpm, few-layer $Ti_3C_2T_x$ suspension with concentration of ~ 1.5 mg ml⁻¹ was prepared.

4.3. Preparation of few-layer Nb₂CTₓ suspension

A total of 3.0 g of Nb_2AlC powder was added gradually (in the course of 5 min) to 30 mL of 50 wt % HF while stirring. The mixture was heated and held at 30 °C for 24 h in an oil bath. Subsequently, the mixture was washed five times via centrifugation. The obtained wet sediment was dispersed in 60 mL of 1 wt% tetramethylammonium hydroxide (TMAOH) solution for 6 h at room temperature. Then the resultant wet sediment was washed via centrifugation and the few-layer Nb_2CT_x suspension with concentration of ~ 1.0 mg ml⁻¹ was obtained.

4.4. Fabrication of hybrid Ti₃C₂Tₓ/Nb₂CTₓ films

Few-layer Nb_2CT_x and $Ti_3C_2T_x$ suspensions were separately mixed in certain weight ratios, yielding a series of hybrid $Ti_3C_2T_x/Nb_2CT_x$ suspensions with different initial Ti3C2Tx contents (5, 10, 30, 50 wt %). Subsequently, each hybrid $Ti_3C_2T_x/Nb_2CT_x$ suspension was filtered using a polypropylene membrane (Celgard, pore size 0.064 μm). After drying, the hybrid $Ti_3C_2T_x/Nb_2CT_x$ films were peeled easily from the membrane, and labeled as 5% T-N, 10% T-N, 30% T-N and 50% T-N according to the Ti3C2Tx contents, respectively.

4.5. Assembly of the symmetric supercapacitors

The symmetric supercapacitors in 2 M H_2SO_4 were assembled with two flexible 30% T-N films with the exact same size of 0.8*3.0 cm² separated by a Celgard membrane used as separator. The all-solid-

state symmetric supercapacitors were assembled with two flexible 30% T-N films with the exact same size of 0.8*3.0 cm², in which PVA-H_2SO_4 gel served as separator and electrolyte. The PVA-H_2SO_4 gel electrolyte was prepared as follows: Approximately 3 g of PVA was dispersed into 30 mL of deionized water at 90 °C with constant stirring until a transparent solution of PVA was obtained. Then 3 g of H_2SO_4 was added to the PVA solution and stirred gently to obtain homogeneous PVA-H_2SO_4 gel electrolyte.

4.6. Assembly of the integrated self-powered sensing devices

The flex sensor (RB-02S046, Suzhou changxian optoelectronic technology co. LTD) with size of 1.0*9.0 cm² was connected in series with the assembled all-solid-state supercapacitor using conductive silver paint to fabricate the integrated self-powered flex sensor. The flex sensor is a polymer thick film device, which is basically a variable resistor that reacts to bends, which resistance increases with the increasing bending degree.

4.7. Materials characterizations

The nanomaterial phases were characterized using a powder X-ray diffractometer (XRD, Bruker, D8 ADVANCE) with Cu Kα radiation (λ = 0.15406 nm). The morphology of the nanomaterials was confirmed using a MEGALLAN 400 scanning electron microscope (SEM) and a transmission electron microscope (TEM) (JEOL JEM-2100, Japan), with an accelerating voltage of 200 kV. The TEM samples were prepared by placing several drops of the material dispersion in alcohol onto a copper grid and air drying. The ICP analysis was conducted to measure the Ti and Nb contents in the hybrid films. The BET nitrogen adsorption-desorption isotherms were used to evaluate the surface area.

4.8. Electrochemical measurements

All the electrochemical tests (cyclic voltammetry (CV), galvanostatic charge/discharge (GCD), electrochemical impedance spectroscopy (EIS) and galvanostatic cycling) were evaluated using an electrochemical workstation (CHI 760e). The electrochemical performance of the hybrid $Ti_3C_2T_x/Nb_2CT_x$ films were measured first with three-electrode Swagelok cells, where the hybrid $Ti_3C_2T_x/Nb_2CT_x$ films (5 mm-diameter disks with mass loadings of 0.6, 2.4 and 3.2 mg cm⁻², respectively) were directly used as the working electrode, overcapacitive activated carbon was the counter electrode, a $Hg/HgSO_4$ electrode was used as the reference electrode, and 2 M H_2SO_4 aqueous solution was the electrolyte. Electrochemical impedance spectroscopy was performed at open circuit potential, with a 10-mV amplitude, and frequencies that ranged from 10 mHz to 100 kHz. The current signal of the integrated flex sensor was measured using CHI760E electrochemical workstation, where the amperometric i-t curve technique was selected.

Gravimetric capacitance (C_m) can be calculated from the CV curves according to the following equation:

$$C_m = \frac{S}{2mvU} \quad (1)$$

where S is the integrating area of the CV curve, m is the mass of the hybrid film electrode, v is the scan rate, and U is the potential window.

The gravimetric energy densities (E_M) as well as power density (P_M) were calculated according to the following equations:

$$E_M = \frac{1}{2}C_MU^2 \quad (2)$$

$$P_M = \frac{E_M}{\Delta t} \quad (3)$$

where Δt is the discharge time. C_M, E_M and P_M are calculated taking into account the total weight of both electrodes (M).

The detailed process to obtain the capacitive control contribution using Dunn's differentiation method is described in SI.

Conflicts of interest

There are no conflicts to declare.

Acknowledgements

References

1 Y. Wang, Y. Song and Y. Xia, *Chem. Soc. Rev.,* 2016, *45,* 5925-5950.
2 K. Jost, G. Diona and Y. Gogotsi, *J. Mater. Chem. A,* 2014, *2,* 10776-10787.
3 V. Augustyn, P. Simon and B. Dunn, *Energ. Environ. Sci.,* 2014, *7,* 1597-1614.
4 B. Mendoza-Sánchez and Y. Gogotsi, *Advanced Materials,* 2016, *28,* 6104-6135.
5 M. Naguib, O. Mashtalir, J. Carle, V. Presser, J. Lu, L. Hultman, Y. Gogotsi and M. W. Barsoum, *ACS Nano,* 2012, *6,* 1322-1331.
6 M. Naguib, M. Kurtoglu, V. Presser, J. Lu, J. J. Niu, M. Heon, L. Hultman, Y. Gogotsi and M. W. Barsoum, *Advanced Materials,* 2011, *23,* 4248-4253.
7 B. Anasori, M. R. Lukatskaya and Y. Gogotsi, *Nat. Rev. Mater.,* 2017, *2,* 16098.
8 M. Alhabeb, K. Maleski, B. Anasori, P. Lelyukh, L. Clark, S. Sin and Y. Gogotsi, *Chemistry of Materials,* 2017, *29,* 7633-7644.
9 O. Mashtalir, M. R. Lukatskaya, M.-Q. Zhao, M. W. Barsoum and Y. Gogotsi, *Advanced Materials,* 2015, *27,* 3501-3506.
10 O. Mashtalir, M. Naguib, V. N. Mochalin, Y. Dall'Agnese, M. Heon, M. W. Barsoum and Y. Gogotsi, *Nat. Commun.,* 2013, *4,* 1716.
11 M. R. Lukatskaya, S. Kota, Z. Lin, M.-Q. Zhao, N. Shpigel, M. D. Levi, J. Halim, P.-L. Taberna, M. W. Barsoum, P. Simon and Y. Gogotsi, *Nat. Energy,* 2017, *2,* 17105.
12 J. Halim, S. Kota, M. R. Lukatskaya, M. Naguib, M.-Q. Zhao, E. J. Moon, J. Pitock, J. Nanda, S. J. May, Y. Gogotsi and M. W. Barsoum, *Advanced Functional Materials,* 2016, *26,* 3118-3127.
13 J. Li, X. Yuan, C. Lin, Y. Yang, L. Xu, X. Du, J. Xie, J. Lin and J. Sun, *Adv. Energy Mater.,* 2017, *7,* 1602725.
14 S. Xu, Y. Dall'Agnesea, G. Wei, C. Zhang, Y. Gogotsi and W. Han, *Nano Energy,* 2018, *50,* 479-488.
15 Chenhui Yang, Y. T., Yapeng Tian, Yangyang Luo, Xingtian Yin, and Wenxiu Que, *ACS Appl. Energy Mater.,* 2020, *3,* 586-596.
16 Y. Tian, W. Que, Y. Luo, C. Yang, X. Yin and L. B. Kong, *J. Mater. Chem. A,* 2019, *7,* 5416-5425.
17 M. Zhu, Y. Huang, Q. Deng, J. Zhou, Z. Pei, Q. Xue, Y. Huang, Z. Wang, H. Li, Q. Huang and C. Zhi, *Adv. Energy Mater.,* 2016, *6,* 1600969.
18 X. Zhao, M. Liu, Y. Chen, B. Hou, N. Zhang, B. Chen, N. Yang, K. Chen, J. Li and L. An, *J. Mater. Chem. A,* 2015, *3,* 7870-7876.
19 M. Ghidiu, M. R. Lukatskaya, M. Q. Zhao, Y. Gogotsi and M. W. Barsoum, *Nature,* 2014, *516,* 78-81.
20 S. Xu, G. Wei, J. Li, Y. Ji, N. Klyui, V. Izotov and W. Han, *Chemical Engineering Journal,* 2017, *317,* 1026-1036.
21 M.-Q. Zhao, C. E. Ren, Z. Ling, M. R. Lukatskaya, C. Zhang, K. L. V. Aken, M. W. Barsoum and Y. Gogotsi, *Advanced Materials,* 2015, *27,* 339-345.
22 Z. Fan, Y. Wang, Z. Xie, D. Wang, Y. Yuan, H. Kang, B. Su, Z. Cheng and Y. Liu, *Adv. Sci.,* 2018, *5,* 1800750.
23 J. Yan, C. E. Ren, K. Maleski, C. B. Hatter, B. Anasori, P. Urbankowski, A. Sarycheva and Y. Gogotsi, *Advanced Functional Materials,* 2017, *27,* 1701264.
24 Z. Ling, C. E. Ren, M.-Q. Zhao, J. Yang, J. M. Giammarco, J. Qiu, M. W. Barsoum and Y. Gogotsi, *P. Natl. Acad. Sci. USA,* 2014, *111,* 16676-16681.
25 F. Shahzad, M. Alhabeb, C. B. Hatter, B. Anasori, S. M. Hong, C. M. Koo and Y. Gogotsi, *Science,* 2016, *353,* 1137-1140.
26 S. Xu, G. Wei, J. Li, W. Han and Y. Gogotsi, *J. Mater. Chem. A,* 2017, *5,* 17442-17451.
27 M. Boota, B. Anasori, C. Voigt, M.-Q. Zhao, M. W. Barsoum and Y. Gogotsi, *Advanced Materials,* 2016, *28,* 1517-1522.
28 W. Tian, A. VahidMohammadi, M. S. Reid, Z. Wang, L. Ouyang, J. Erlandsson, T. Pettersson, L. Wagberg, M. Beidaghi and M. M. Hamedi, *Advanced Materials,* 2019, *31,* 1902977.
29 S. Xu, Y. Dall'Agnese, G. Wei, C. Zhang, Y. Gogotsi and W. Han, *Chem.-Eur. J.,* 2018, *24,* 18556-18563.
30 C. Zhang, S. J. Kim, M. Ghidiu, M.-Q. Zhao, M. W. Barsoum, V. Nicolosi and Y. Gogotsi, *Advanced Functional Materials,* 2016, *26,* 4143-4151.
31 A. Byeon, A. M. Glushenkov, B. Anasori, P. Urbankowski, J. Li, B. W. Byles, B. Blake, K. L. Van Aken, S. Kota, E. Pomerantseva, J. W. Lee, Y. Chen and Y. Gogotsi, *J. Power Sources,* 2016, *326,* 686-694.
32 J. Luo, W. Zhang, H. Yuan, C. Jin, L. Zhang, H. Huang, C. Liang, Y. Xia, J. Zhang, Y. Gan and X. Tao, *ACS Nano,* 2016, *11,* 2459-2469.
33 M. Naguib, J. Halim, J. Lu, K. M. Cook, L. Hultman, Y. Gogotsi and M. W. Barsoum, *J. Mater. Chem. A,* 2013, *135,* 15966-15969.
34 J. Xiao, J. Wen, J. Zhao, X. Ma, H. Gao and X. Zhang, *Electrochim. Acta,* 2020, *337,* 135803.
35 Q. Shan, X. Mu, M. Alhabeb, C. E. Shuck, D. Pang, X. Zhao, X.-F. Chu, Y. Wei, F. Du, G. Chen, Y. Gogotsi, Y. Gao and Y. Dall'Agnese, *Electrochemistry Communications,* 2018, *96,* 103-107.
36 A. K. Geim and I. V. Grigorieva, *Nature,* 2013, *499,* 419-425.
37 K. S. Novoselov, A. Mishchenko, A. Carvalho and A. H. Castro Neto, *Science,* 2016, *353,* aac9439.
38 E. Pomerantseva and Y. Gogotsi, *Nat. Energy,* 2017, *2,* 17089.
39 Y. Liu, N. O. Weiss, X. Duan, H.-C. Cheng, Y. Huang and X. Duan, *Nat. Rev. Mater.,* 2016, *1,* 16042.
40 V. Augustyn, J.Come, M. A. Lowe, J. W. Kim, P. L. Taberna, S. H. Tolbert, H. D. Abruna, P. Simon and B. Dunn, *Nature materials,* 2013, *12,* 518-522.
41 X. Mu, D. Wang, F. Du, G. Chen, C. Wang, Y. Wei, Y. Gogotsi, Y. Gao and Y. Dall'Agnese, *Advanced Functional Materials,* 2019, *29,* 1902953.
42 M. Khazaei, A. Ranjbar, M. Arai, T. Sasaki and S. Yunoki, *J. Mater. Chem. C,* 2017, *5,* 2488-2503